

Abstract

The major ice caps in the late Ordovician lay between the base of the *N. extraordinarius* biozone and lower part of the *N. persculptus* biozone, consistent with the low values of CIA, CIW and PIA for the Huadi No. 1 well, reflecting a short-lived cold and dry climate from the top of the Wufeng-Guanyinqiao Formation to the base of the Longmaxi Formation in the Huadi No. 1 well. These observations provide geochemical record evidence for Gondwana glaciation at the end of the Ordovician in South China.

Keywords

Glaciation • Gondwana glaciation • Geochemistry • Hirnantian period • Shale gas

The Late Ordovician-Early Silurian transition was a critical interval in Earth's history, marked by global eustasy, climate cooling (Gondwana glaciation), volcanic eruption, ocean anoxia and biotic mass extinction. These geological events considerably influenced the sedimentation of shales in the Wufeng-Longmaxi Formations, which controlled the formation and distribution of favorable shale gas intervals (Qiu and Zou 2020). In this chapter, we study the Gondwana glaciation.

5.1 The Continental Glacial Activity of Late Ordovician

At the end of the Late Ordovician, large-scale continental glacier activities occurred globally. Geological scholars in France and Algeria first reported the tillites and glacial stria of the Ashgillian stage in the central Sahara. Later, records of continental or marine glacier activities in the late Ordovician, North Africa, South Africa, Southern Europe, Central Europe, West Asia and South America were

discovered. The glaciers in this period were part of the Gondwana glacier that surrounded the Antarctic region at that time, centered in North Africa, and extending to South Africa, southern and central Europe, West Asia and South America. Such a large area of glacial activity can reflect the global paleoclimate and paleogeographic characteristics at that time, which has geological significance (Rong and Zhan 1999). In Morocco and Libya, glacier-related strata developed the atypical Hirnantian fauna and were overlain by graptolite strata of the *Parakidograptus acuminatus* zone; thus, these strata were identified in the late Ashgill stage, with a duration of only approximately 50×10^4 – 100×10^4 a. Although South China was located near the equator at the end of the Late Ordovician, no direct evidence (such as tillites and glacial scratches) has been found for this glaciation in China, and most scholars agree that this glaciation indirectly influenced South China (in the form of sea-level fluctuations, paleoclimate changes, biofacies and paleogeographic characteristics). The formation of ice caps and change in the carbon and oxygen isotope composition in seawater were the characteristic factors for the first pulse of the end Ordovician mass extinction. The average reduction in the global atmospheric and ocean temperatures was 8–10 °C. Most of the sea areas in the late Ashgill turned into cold water areas, which influenced the plankton (graptolites), swimming organisms (trilobites and cephalopods) and benthic organisms (brachiopods and corals) developed in the relatively warm sea areas in the middle of Ashgill. The cold waters with high density in the high latitudes migrated toward the equator, causing cold, deep-water currents with oxygen and nutrients to flow into the waters and ocean currents to overturn. Considerable changes occurred in the ecosystems of the previously formed deeper, oxygen-poor and nutrient-poor waters, resulting in the extinction of the Foliomena fauna, and the subsequent warming of the atmospheric and sea temperatures led to the melting of the ice sheet, which was the characteristic factor for the second pulse of the end Ordovician mass extinction. The rapid rise

All samples were ground and cleaned with distilled water, then dried and ground to 200 mesh for analytical testing.

The Upper Ordovician-Early Silurian succession in Well Huadi No.1 includes three successive formations: the Wufeng, Guanyinqiao and Longmaxi Formations in ascending order (Fig. 5.1). Wufeng Formation is in conformable contact with the underlying Linxiang Formation. The lithology of Linxiang Formation is mainly gray and dark gray nodular argillaceous limestone with a small amount of brachiopods, trilobites and other organisms. Pyrite aggregates are developed in the limestone, and asphalt can be seen near the bottom. This formation has a depth range of 1337.2–1339.86 and a thickness of about 2.66 m.

The depth of Wufeng Formation ranges from 1331.87 to 1337.2 m, and the lithology is mainly gray-black to black carbonaceous mudstone and carbonaceous siliceous mudstone. Four bentonite beds, about 0.5–1 cm thick each layer, were discovered in the black shales with graptolite and brachiopods fossils. Pyrite veins developed in the bottom of Wufeng Formation and generally parallel to the bedding.

The depth of Guanyinqiao Formation ranges from 1330.37 to 1331.87 m, and the thickness is about 1.5 m. The petrology is dark gray argillaceous siltstone. Silty bands are well developed and distributed in grayish white lamellar on the plane (Fig. 5.2). Lenticular pyrites are commonly developed in the bentonites.

Fig. 5.2 Brief sectional structure of the Wufeng-Longmaxi Formations in the Well Huadi no. 1

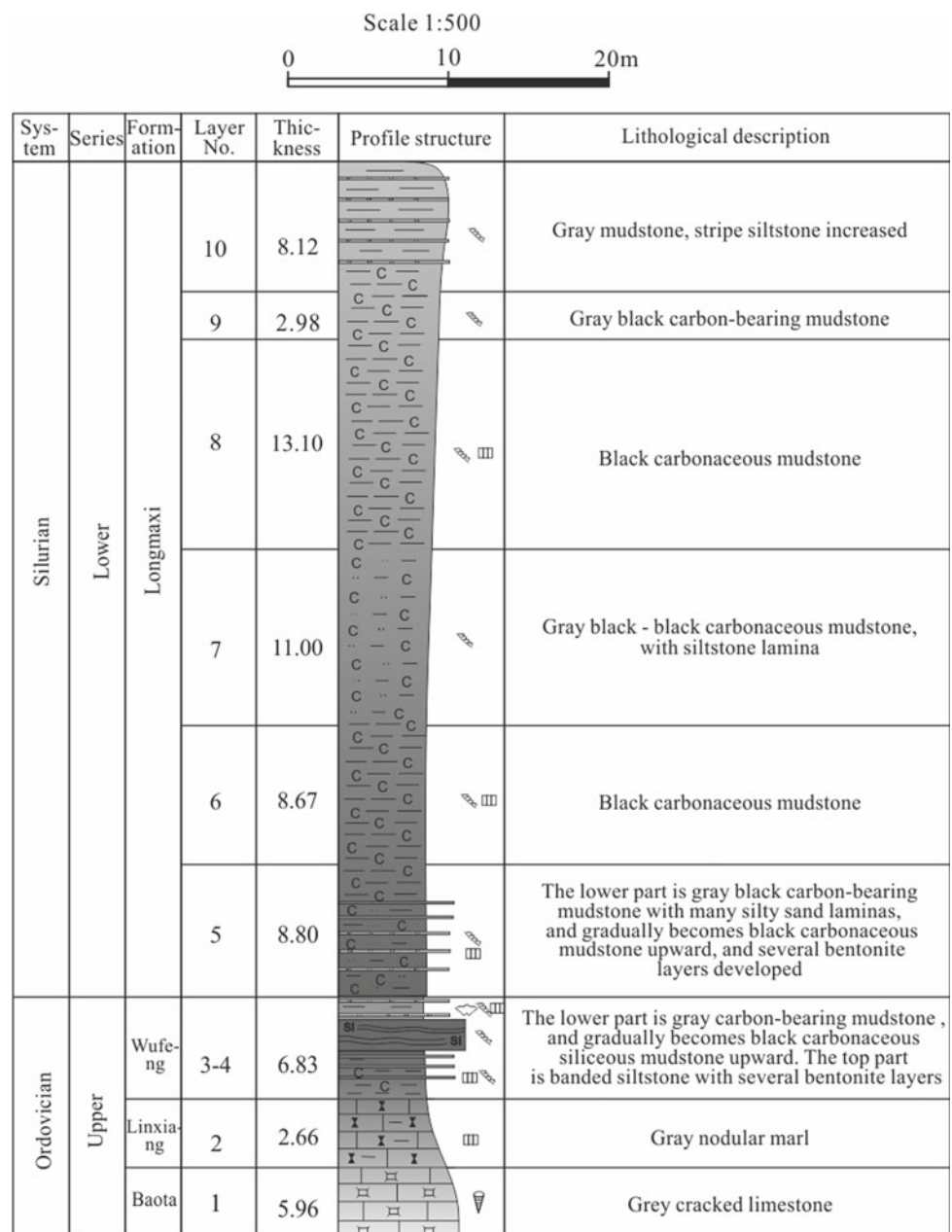
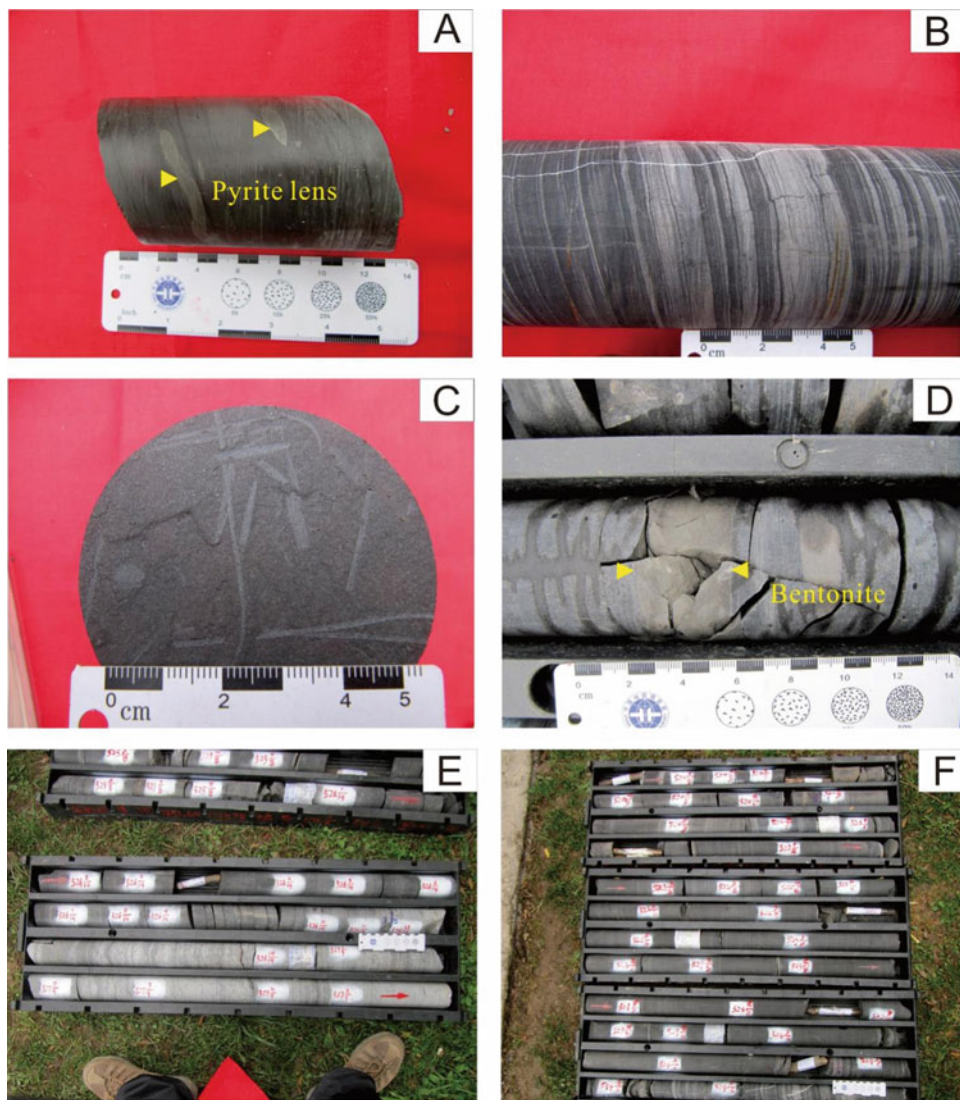


Fig. 5.3 Field photograph characteristics of the Wufeng-Longmaxi Formations in the Well Huadi no. 1. **a** Pyrite occurs as lenses in the black shales of the Wufeng Formation. **b** Laminar structure of siltstones in the Guanyinqiao Formation. **c** Graptolites developed in Longmaxi Formation. **d** Bentonites deposited in Longmaxi Formation. **e** Boundary between the Wufeng to Guanyinqiao Formation. **f** Macrocharacteristics of Guanyinqiao-Longmaxi Formations



The depth range of Longmaxi Formation is 726.56–1330.37 m, and the thickness is about 603.81 m. According to the changes of rock lithology and color, the Longmaxi Formation can be divided into two parts. The lower part of Longmaxi Formation, namely the most favorable black shale section, roughly ranges from 1321 to 1330.37 m, and the lithology of this part is mainly gray black to black carbonaceous shale. Numerous bentonites were discovered in the shales with thickness of 1–2 cm and maximum thickness of 3 cm. Occasionally, there are silty bands with horizontal laminar texture. Graptolites, mainly fine and straight graptolites, were abundantly developed in the shales. The pyrite can be found in Longmaxi Formation as veins and disseminated fine particles. The upper part of Longmaxi Formation mainly contains dark gray, gray-green, carbon-bearing silty mudstone and siltstone. The whole part is manifested by the gradual process of rock lithology and color. The color changes from dark grey to gray-green. The increasing silty

contents make the rocks shift from carbon-bearing silty mudstones to mudstones and muddy siltstones rhythm then to siltstones. Near the top numerous limestone, biological limestone interbeds are discovered in the siltstones. The biological particles are mainly crinoids, brachiopods and oolitic particles, and there are wormtrails in siltstone. The changes of lithologic and sedimentary structure characteristics from bottom to top in Longmaxi Formation indicate the process of paleoseawater depth from deep to shallow (Fig. 5.3).

5.2.2 The Lithology of Wufeng-Longmaxi Formations in the Well Huadi No. 1

According to the thin section and X-ray diffraction analyses, the black shales of the Wufeng and Longmaxi Formations have pelitic textures and are composed mainly of clastic

Table 5.1 Mineral compositions of samples from Wufeng-Longmaxi Formations in Well Huadi no. 1 (XRD)

No.	Sample	Clay mineral relative content (%)							Whole rock analysis (%)										
		K	C	I	S	I/S	C/S		Interlaying	Clay miner-als		Quart-z	Orthoclase	Albite	Pyrite	Calcite	Dolomite	Pyroxenes	
								I/S	C/S										
1	HDP-B1	2	1	20	/	75	2	8	12	38.7		38.9	0.7	5.6	0.7	6.1	9.3	\	\
2	HDP-B2	2	1	13	/	82	2	7	12	36.7		35.4	\	5	\	1.6	14.5	\	\
3	HDP-B4	2	1	14	/	82	1	8	14	28.1		41.1	1.3	7	1.3	\	14.2	2.8	2.8
4	HDP-B7	2	1	16	/	78	3	7	16	31.5		40.0	\	4	\	0.3	20.1	\	\
5	HDP-B10	1	1	22	/	72	4	6	16	33.6		53.6	\	5	\	\	4.3	\	\
6	HDP-B18	/	/	34	/	66	/	6	/	10.8		85.0	\	1.4	\	\	\	\	\
7	HDP-B19	/	/	25	/	75	/	7	/	71.8		12.5	\	1.5	\	\	\	\	\
8	HDP-B21	2	2	18	/	74	4	10	18	25.8		53.1	1.0	10.3	1.0	2.7	3.4	\	\
9	HDP-B23	1	2	16	/	78	3	8	13	25.1		47.0	0.8	12.3	0.8	3.6	4.5	\	\
10	HDP-B25	1	1	15	/	76	7	8	12	28.3		39.5	1.9	11.1	1.9	1.8	11	\	\
11	HDP-B26	1	3	14	/	76	6	7	15	31		39.7	0.9	10.7	0.9	5	8.6	\	\
12	HDP-B29	1	2	14	/	80	3	7	13	26.5		36.6	0.7	9.5	0.7	0.7	23.8	\	\
13	HDP-B30	1	2	13	/	79	5	8	9	32.3		42.8	1.9	10.9	1.9	2	6.1	\	\
14	HDP-B31	/	/	11	/	89	/	8	/	46		43.5	\	0.8	\	0.3	\	\	\
15	HDP-B33	1	2	14	/	79	4	9	9	25.3		43.5	1.8	15.2	1.8	1.4	9.5	\	\
16	HDP-B34	1	2	16	/	77	4	9	10	25.5		33.7	1.3	10.6	1.3	14	11.5	\	\

K Kaolinite; C Chlorite; I Illite; S Montmorillonite

particles (quartz, feldspar) and clay minerals. The clay minerals with microscale pelitic texture are directionally arranged in the rocks. A part of the clay minerals renders the organic matter as scale aggregates along the bedding, and other minerals fill the small cracks as black bands. Radiolarians can be found in mudstones of the Wufeng Formation, which have an elliptical shape with a diameter of 60–120 μm . The cements are mainly calcite and dolomite, among which dolomites occur as euhedral crystals, while calcite is mostly microcrystalline and distributed in clay minerals. The siltstone of the Guanyinqiao Formation exhibits alternating layers of quartz particles and clay minerals.

The X-ray diffraction (XRD) results of 16 samples from the Wufeng-Longmaxi Formations in the Well Huadi No. 1 (Table 5.1) indicate that quartz is the dominant mineral in the black shales of the Wufeng and Longmaxi Formations.

Quartz contents range from 33.6 to 53.6% with an average value of 42.9%, whereas the clay mineral contents have an average value of 31.0% with a range of 25.1–46%. Microcline (0–1.9%), albite (0.8–15.2%), calcite (0–14.1%), dolomite (0–23.8%), and pyrite (0.7–9.4%) contents in the black shales are low. The clay minerals are mainly composed of mixed-layer illite/smectite (72–89%, avg. 78.4%) and illite (11–22%, avg. 15.4%) (Figs. 5.4 and 5.5). The contents of both chlorite and mixed-layer chlorite/smectite are less than 10%, with values of 1–3% and 1–7%, respectively.

The quartz contents in the siltstones of the Guanyinqiao Formation range from 12.5% to 85.0%, and the clay mineral contents range from 10.8% to 71.8%. The clay minerals are dominated by illite (25–34%) and illite/smectite mixed layers (66–75%). The second-most abundant minerals are pyrite (2.8–14.2%) and albite (1.4–1.5%).

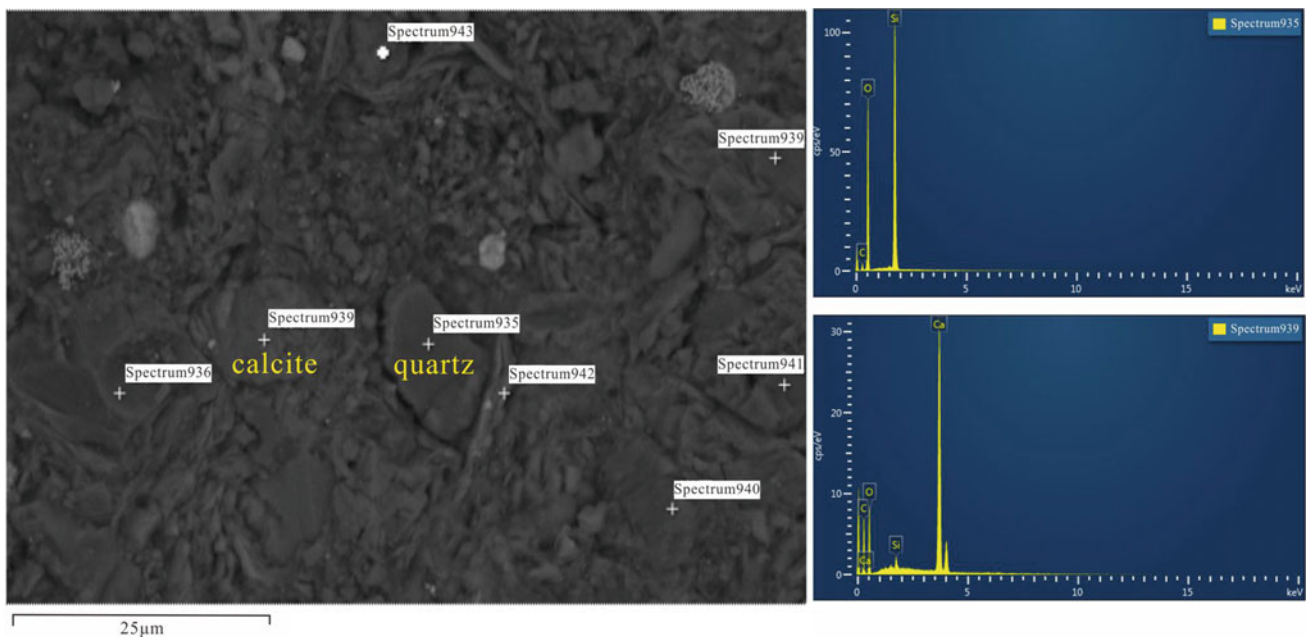


Fig. 5.4 Spectrum diagram of studied sample B36 of Longmaxi Formation

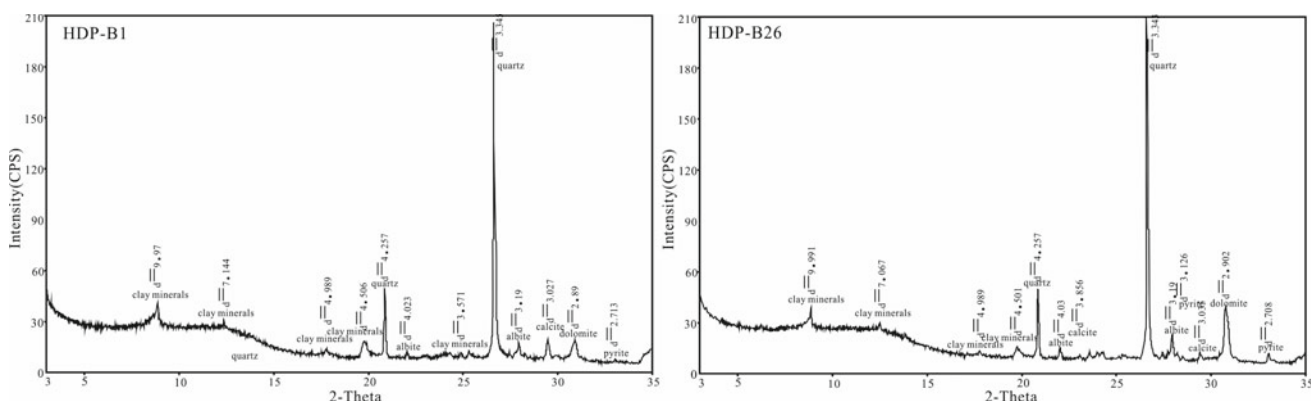


Fig. 5.5 XRD patterns of the black shales of Wufeng and Longmaxi Formations in Well Huadi no. 1

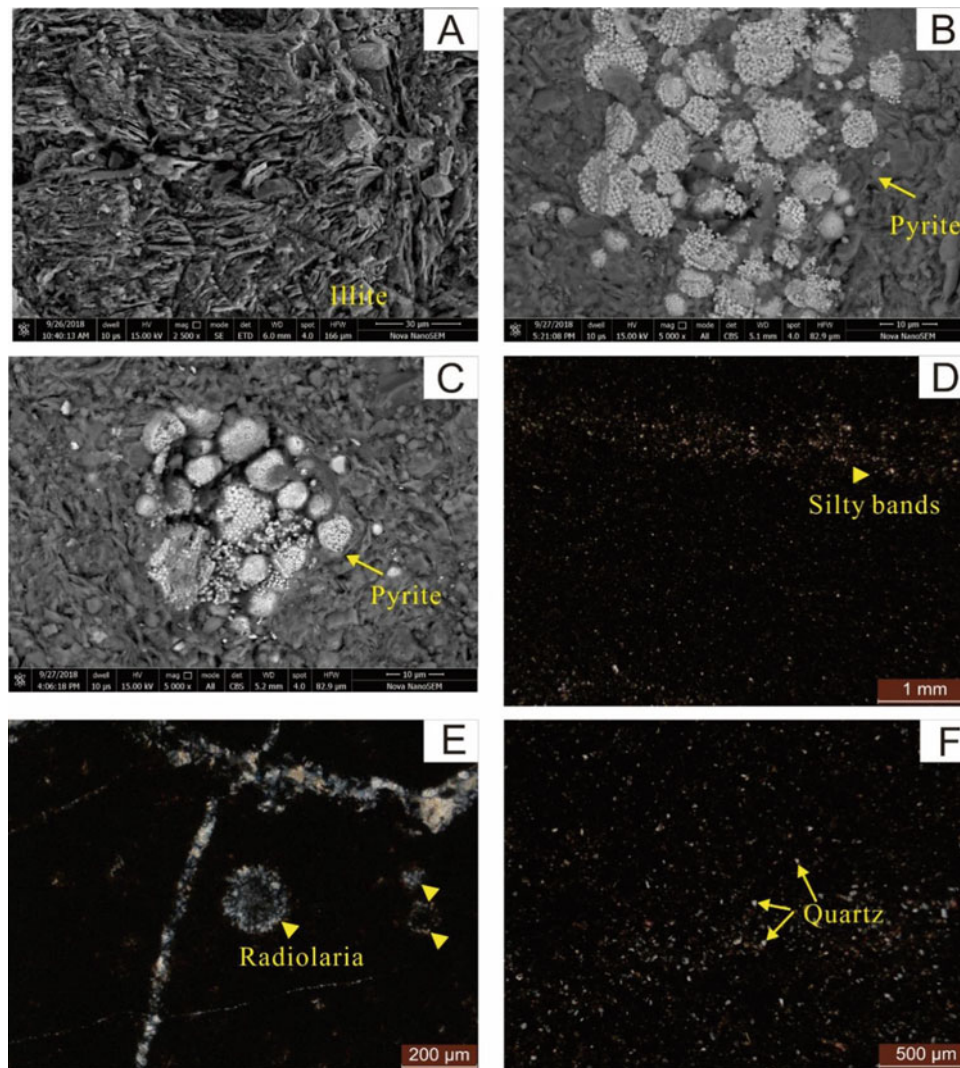


Fig. 5.6 Microcharacteristics of black shales from Wufeng-Longmaxi Formations in Well Huadi No. 1. **a** Scanning electron microscopy image of B17 clay minerals in the black shales of Wufeng Formation; **b** scanning electron microscopy image of the sample B30 in the black shales of Longmaxi Formation: pyrite framboids; **c** scanning electron

microscopy image of the sample B15 of Wufeng Formation: pyrite framboids; **d** the horizontal silty bands developed in the black shales of Longmaxi Formation; **e** radiolarian developed in black shales of Wufeng Formation (sample B13); **f** the microscopic characteristics quartz (round-oval shape) in the shales of Longmaxi Formation

The scanning electron microscopy images of the black shales of the Wufeng and Longmaxi Formations show that the pyrites are characterized by euhedral and subhedral fabrics and exist as framboids with a particle diameter of 1–8 μm (Fig. 5.6).

5.2.3 The Geochemical Characteristics of the Wufeng-Longmaxi Formations from the Well Huadi No. 1

The major element concentrations of the 34 samples from Wufeng-Longmaxi Formations in Well Huadi No.1 are listed in Tables 4.47, 5.3. For the black shales and mudstones

in the Wufeng Formation, SiO_2 (38.26–91.18%) and Al_2O_3 (1.49–15.48%) are the most abundant oxides. According to the results from the XRD measurements, the mineral compositions of shales from the Wufeng Formation are dominated by quartz and clays, which is in accordance with the chemical compositions. The second most abundant oxides are CaO (0.548%–10.92%), Fe_2O_3 (0.961–7.75%), and K_2O (0.324–4.13%). The concentration of MgO in the shales is 0.554–6.74%. The FeO content of the black mudstones (0.7–2.11%) is slightly lower than the Fe_2O_3 content, while other oxide contents, including those of Na_2O , P_2O_5 , TiO_2 , and MnO , are lower than 1.0%.

The SiO_2 content of the Guanyinqiao siltstones ranges from 30.09 to 56.61%. The second-most abundant oxide is

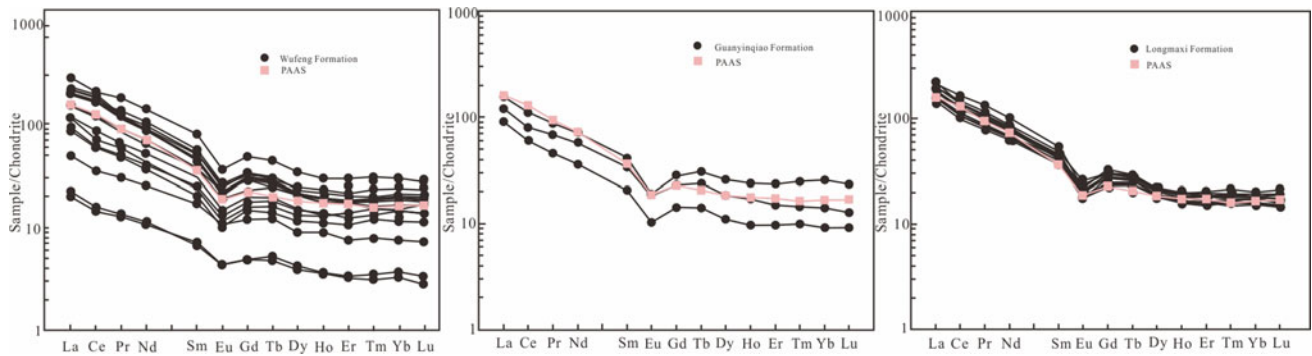


Fig. 5.7 Chondrite-normalized REE distribution patterns of samples from Wufeng-Longmaxi Formations in Huadi no. 1 well (normalization values after Taylor and McLennan 1985)

CaO (8.07–29.81%), the content of which is higher than that of Al_2O_3 (3.22–9.49%). The contents of Fe_2O_3 and FeO are 3.1–4.05 and 0.69–1.23%, respectively. The concentration of MgO is 1.23–3.02%, while the contents of other oxide, such as Na_2O , P_2O_5 , TiO_2 , and MnO, are equal to or less than 1%.

The shale samples in the Longmaxi Formation are characterized by a dominance of SiO_2 (42.09–65.72%), and Al_2O_3 follows SiO_2 in abundance (8.14–13.64%). The third-most abundant oxide is CaO (2.01–12.22%), with an average value of 5.68%. The contents of Fe_2O_3 (3.40–6.03%, avg. 4.34%), FeO (0.91–2.3%, avg. 1.56%) and K_2O (1.8–3.33%, avg. 2.73%) are close to the average values of the black shales in the Wufeng Formation [Fe_2O_3 (avg. 4.22%), FeO (avg. 2.11%) and K_2O (avg. 2.71%)]. The Na_2O (0.856–1.49%, avg. 1.30%) and MgO (1.57–7.29%, avg. 3.16%) contents are slightly higher than those of the Wufeng Formation shales (avg. 0.52 and 2.00%, respectively). The concentrations of MnO (0.016–0.181%), TiO_2 (0.442–0.621%) and P_2O_5 (0.101–0.281%) are lower than 1%.

Compared with the post-Archean average shale (PAAS) values (Taylor and McLennan 1985), the shales from the Wufeng Formation have slightly higher SiO_2 (avg. 65.92%) and CaO (avg. 2.91%) contents. In addition, the Al_2O_3 (avg. 10.26%) and K_2O (avg. 2.71%) contents are lower than those of the PAAS, which indicates that the content of the clay minerals is low in the samples. Fe_2O_3 , MnO, Na_2O , P_2O_5 and TiO_2 are slightly depleted in the shales relative to the PAAS.

The shales from the Longmaxi Formation are enriched in Na_2O and CaO and slightly to strongly depleted in terms of the other major elements (SiO_2 , Al_2O_3 , Fe_2O_3 , K_2O , P_2O_5 , TiO_2 and MnO). The SiO_2 (avg. 56.49%) and Al_2O_3 (avg. 11.34%) deficits indicate a decrease in the amount of clay minerals. The enrichment of Na_2O (avg. 1.3%) and CaO (avg. 5.68%) relative to the PAAS can be attributed to the presence of plagioclase and secondary calcite in caliches (Lee 2009), while the depletion of TiO_2 (avg. 0.55%) and

K_2O (avg. 2.73%) suggests that phyllosilicate minerals exist in lesser quantities in the shales (Condie et al. 1992; Moosavirad et al. 2011).

The siltstones from the Guanyinqiao Formation are enriched in CaO and slightly depleted in other major elements (SiO_2 , Al_2O_3 , Fe_2O_3 , K_2O , P_2O_5 , TiO_2 and MnO). The concentration of P_2O_5 (avg. 0.17%) is similar to that of the PAAS (0.16%).

The total rare earth element contents (ΣREE) from the Wufeng Formation show significant variability ($27.17\text{--}334.01 \times 10^{-6}$), with an average of 168.30×10^{-6} (Table 4.48), which is lower than that of the PAAS (184.77 ppm; Taylor and McLennan 1985). The light rare earth element (LREE) contents ($21.23 \times 10^{-6}\text{--}299.83 \times 10^{-6}$, avg. 149.99×10^{-6}) are apparently higher than those of the heavy rare earth elements (HREEs) ($3.66 \times 10^{-6}\text{--}34.18 \times 10^{-6}$, avg. 18.31×10^{-6}), and the mean LREE/HREE ratio is 5.80–11.29. The (La_N/Yb_N) ratio is 6.09–12.07. The Eu/Eu* value is 0.53–0.75. In the chondrite-normalized REE distribution patterns diagram, we can see that the LREE and HREE contents of the samples are slightly lower than those of PAAS. All samples exhibit similar REE distribution curves, showing slight LREE enrichment and relatively flat HREE patterns with weakly negative Eu anomalies. The V-type right-inclining REE distribution model is similar to the granite's, suggesting that the source rocks of Wufeng, Guanyinqiao and Longmaxi Formations are felsic (Fig. 5.7).

5.2.4 The Paleoweathering of the Late Ordovician-Early Silurian Transition in Well Huadi No. 1 and the Implications for the Paleoclimate

During rock chemical weathering processes, chemical weathering increases under humid conditions, causing the leaching of alkali metal and alkaline metal elements, such as Na, K and Ca, and increased concentrations of Al and Si in

the residue. The most popular paleoweathering indices used to assess the degree of chemical weathering in the source area are the Chemical Index of Alteration (CIA, Nesbitt and Young 1982), Chemical Index of Weathering (CIW, Harnois 1988) and Plagioclase Index of Alteration (PIA, Fedo et al. 1995).

In the CIA index, new potassium elements are introduced in the potassium metasomatism during diagenesis, resulting in a low CIA value, and thus, the CIA value needs to be corrected. Based on the A–CN–K ternary diagram, Nesbitt and Young (1984, 1989) obtained the weathering profiles and predicted the weathering trendlines of the sediments by analyzing the thermodynamic and kinetic processes of feldspar decomposition and geochemical characteristics of weathering profiles in nature. As shown in Fig. 4-101-(1), solid lines a and b are nearly parallel to the A–CN line and represent the weathering trend without potassic metasomatism. Solid line c represents the weathering trend with potassic metasomatism. In addition, the dotted distance between solid lines 3 and 4 represents the CIA values of the shales with potassic metasomatism. Fedo et al. (1995) pointed that the intersection between the weathering trend without potassic metasomatism and back extension line of the K apex and samples represents the premetasomatized CIA value (the correction value is the solid line distance between lines 1 and 2 in Fig. 4-101-(1); Mou et al. 2019).

The mobility of elements can be evaluated using an Al_2O_3 –($\text{CaO}^* + \text{Na}_2\text{O}$)– K_2O (A–CN–K) ternary diagram (Nesbitt and Young 1984), where A = Al_2O_3 (mol %), CN = $\text{CaO}^* + \text{Na}_2\text{O}$ (mol%) and K = K_2O (mol%). A–CN–K relationships can be interpreted in terms of the weathering history, paleoclimate and source rock composition (Fedo et al. 1995). The CIA values plotted in an A–CN–K

triangular diagram (Fedo et al. 1996) can clarify the differentiation of compositional changes associated with chemical weathering and source rock composition (Nesbitt and Young 1984). As shown in Fig. 5.6, the samples of the three formations plot above the plagioclase–K-feldspar join and show a narrow linear trend that approaches the A apex. The weathering trends lie subparallel to the A–CN join and do not exhibit any inclination toward the K apex, suggesting that the rocks were not subjected to potash metasomatism during diagenesis. The trendline, when extended backward, intersects the plagioclase–K-feldspar join near the granodiorite and granite fields (potential source rock).

The weathering trends of the samples from the Wufeng-Longmaxi Formations lie subparallel to the A–CN join and do not exhibit any inclination toward the K apex in Fig. 4-101-(2), suggesting that the rocks in the Huadi No. 1 well were not subjected to potash metasomatism during diagenesis. The CIA_{corr} values calculated from the equation are consistent with the original CIA values (Fig. 5.8, Table 4.2).

The CIA values of the Wufeng-Longmaxi Formations in the Huadi No. 1 well exhibit a certain regularity from the bottom to the top, as shown in Fig. 4-102. The CIA values of black shales from the Wufeng Formation first increase and then decrease from the bottom up, ranging from 66.15 to 72.17 (avg. 68.86). At the top of the formation, the values decrease to a trough, with values between 66.15 and 70.35, and upward in the Guanyinqiao Formation, the CIA values decrease, varying between 59.96 and 62.86 (avg. 61.87). At the top of the Guanyinqiao Formation, the values fall to 59.96. Further upward, at the base of the Longmaxi Formation, the CIA rapidly returns to a high value (62.06). The CIA values of the Longmaxi Formation increase

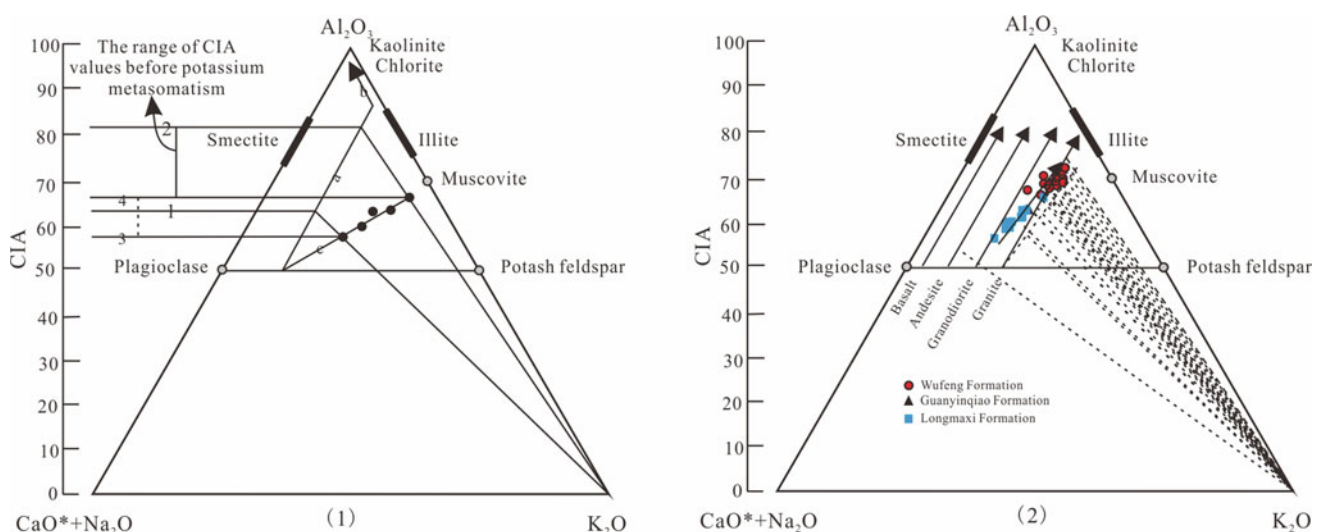


Fig. 5.8 Al_2O_3 – $\text{CaO}^* + \text{Na}_2\text{O}$ – K_2O ternary diagram for samples of Wufeng-Longmaxi Formations in Well Huadi no. 1 (modified by Nesbitt and Young 1984; Fedo et al. 1995)

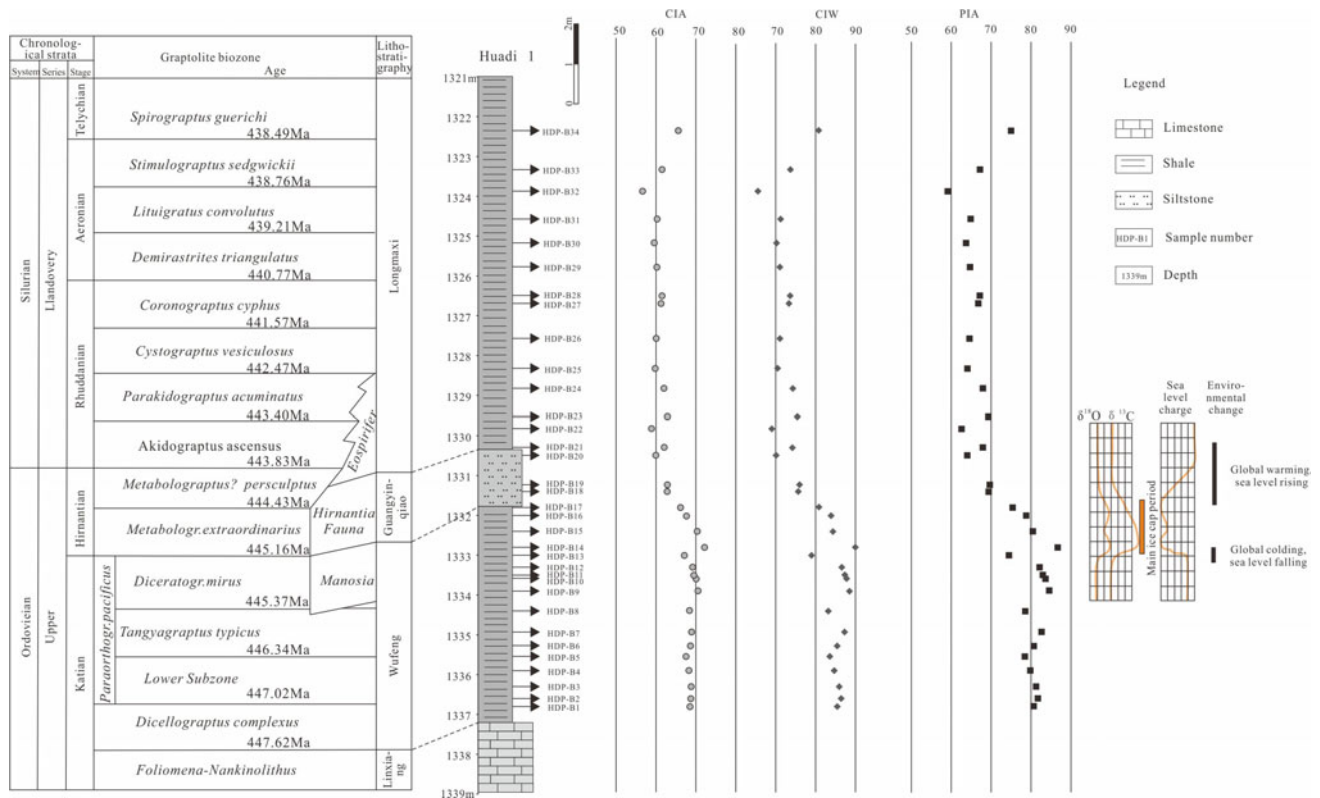


Fig. 5.9 Stratigraphic, lithological correlations and paleoweathering indices of CIA, PIA and CIW of Wufeng and the lower Longmaxi Formations in Well Huadi no. 1 (chronostratigraphic subdivision after

Chen et al. 2017; isotope, sea level and environmental change after Brenchley et al. 2006; Harper et al. 2014)

gradually from the bottom up, ranging from 56.64 to 65.59 (avg. 60.87).

The trends of the PIA and CIW in the Wufeng-Longmaxi Formation are the same as those of the CIA. The CIW and PIA values of the lower Wufeng Formation rocks range from 78.98 to 89.96 and 74.46–86.68, respectively. At the top of this formation, the values fall to 80.84–84.35 and 75.38–80.46 and are higher in the strata. In the Guanyinqiao Formation, the CIW and PIA values decrease, varying from 70.10 to 75.98 (avg. 73.91) and from 64.02 to 69.65 (avg. 67.68), respectively. Further upward, at the base of the Longmaxi Formation, the CIW and PIA promptly return to high values (74.19 and 67.92). The CIA and PIA values of the Longmaxi Formation increase gradually from the bottom to the top, ranging from 65.55 to 80.78 (avg. 72.42) and from 59.12 to 74.99 (avg. 66.06), respectively.

Generally, the variations in the CIA value can indicate the paleoclimate (Nesbitt and Young 1984; Young and Nesbitt 1998; Fedo et al. 1995; Yan et al. 2010; Fu et al. 2015; Ge et al. 2019a, 2019b; Ma et al. 2015). Low CIA values (50–60) are suggestive of cold and arid climatic conditions with weak chemical weathering, moderate CIA values (60–80) indicate warm and humid climate conditions with medium chemical weathering, and high CIA values (80–100) indicate

hot and humid tropical climatic conditions with intensive chemical weathering. Fluctuations in CIA values indicate that the intensity of chemical weathering changed from moderate to weak and then to moderate, and the climate shifted from warm to cold and then to warm again from the base of the Wufeng Formation to the lower part of the Longmaxi Formation in the Huadi No. 1 well (Fig. 5.9, Tables 5.2 and 5.3).

5.2.5 Sedimentary Mode of the Black Shales from Wufeng-Longmaxi Formations in Sichuan Basin

During the late Ordovician-early Silurian, affected by the Caledonian movement, the Cathaysia block collided with the Yangtze Block and expanded constantly. The Central Guizhou, Central Sichuan and Western Sichuan-Central Yunnan uplifts around the Upper Yangtze area constantly expanded, and the Yangtze area developed into the back-bulge basin confined by the marginal uplifts. As the uplifts expanded, the base of the upper Yangtze basin subsided promptly, and the sea level rose. In addition, frequent volcanic eruptions occurred in the middle of the Katian

Table 5.2 Analytical data of major elements (wt%) of shales and siltstones from Wufeng-Longmaxi Formations in Well Huadi no. 1

Sample	HDP-B1	HDP-B2	HDP-B3	HDP-B4	HDP-B5	HDP-B6	HDP-B7	HDP-B8	HDP-B9	HDP-B10	HDP-B11
Wufeng Formation											
SiO ₂	57.02	54.12	56.19	56.27	54.15	53.71	38.26	73.24	69.45	68.59	60.58
Al ₂ O ₃	15.36	15.09	15.48	15.39	14.06	14.23	10.21	8.69	13.35	9.81	13.79
CaO	4.16	4.38	3.1	3.3	4.36	3.68	10.92	1.82	0.647	0.549	2.43
Fe ₂ O ₃	3.3	4.8	5.64	5.3	5.26	6.09	6.92	3.75	3.02	7.75	3.42
FeO	1.19	1.31	0.95	1.05	1.56	1.3	2.11	1.06	1.26	1.23	0.91
Fe ₂ O _{3t}	4.62	6.26	6.70	6.47	6.99	7.53	9.26	4.93	4.42	9.12	4.43
K ₂ O	4.09	4.14	4.13	4.03	3.68	3.75	2.87	2.08	3.54	2.6	3.74
MgO	2.59	2.73	2.2	2.48	2.92	3.18	6.74	1.51	1.17	0.919	2.36
MnO	0.057	0.059	0.041	0.044	0.06	0.065	0.177	0.031	0.018	0.018	0.03
Na ₂ O	0.796	0.721	0.771	0.847	0.841	0.739	0.453	0.534	0.528	0.416	0.608
P ₂ O ₅	0.066	0.069	0.062	0.084	0.099	0.073	0.066	0.08	0.071	0.064	0.1
TiO ₂	0.769	0.726	0.761	0.725	0.693	0.684	0.482	0.407	0.619	0.609	0.49
LOI	9.71	9.01	9.62	9.54	10.79	10.79	18.26	7.57	7	8.1	10.35
Total	99.11	97.16	98.95	99.06	98.47	98.29	97.47	100.77	100.67	100.66	98.81
Al ₂ O ₃ /TiO ₂	19.97	20.79	20.34	21.23	20.29	20.80	21.18	21.35	21.57	16.11	28.14
K ₂ O/Na ₂ O	5.14	5.74	5.36	4.76	4.38	5.07	6.34	3.90	6.70	6.25	6.15
CaO*	0.013	0.012	0.012	0.014	0.014	0.012	0.007	0.009	0.009	0.007	0.010
CIA	68.52	68.73	68.81	68.25	67.53	68.64	68.92	68.40	70.53	70.07	69.48
CIA _{corr}	68.52	68.73	68.81	68.25	67.53	68.64	68.92	68.40	70.53	70.07	69.48
PIA	80.66	81.71	81.26	79.81	78.44	80.69	82.64	78.55	84.55	83.62	82.95
CIW	85.43	86.41	85.92	84.67	83.56	85.41	87.26	83.18	88.49	87.76	87.33
Sample	HDP-B12	HDP-B13	HDP-B14	HDP-B15	HDP-B16	HDP-B17	HDP-B18	HDP-B19	HDP-B20	HDP-B21	HDP-B22
Guanyinqiao Formation											
SiO ₂	68.55	91.18	82.35	91.57	76.47	69.01	30.09	56.61	55.44	63.69	
Al ₂ O ₃	8.36	1.57	3.48	1.49	7.69	6.36	3.22	4.82	9.49	13.43	
CaO	0.559	0.943	1.95	0.885	0.548	5.27	29.81	13.71	8.07	2.01	
Fe ₂ O ₃	7.13	1.09	2.06	0.961	2.01	3.28	3.35	3.1	4.05	3.8	
FeO	0.8	0.7	0.98	0.77	0.84	0.88	0.69	1.22	1.23	0.91	
Fe ₂ O _{3t}	8.02	1.87	3.15	1.82	2.94	4.26	4.12	4.46	5.42	4.81	
K ₂ O	2.21	0.324	0.879	0.324	2.03	1.61	0.803	1.22	2.11	3.26	
MgO	0.791	0.554	1.13	0.49	0.83	1.38	2.2	1.23	3.02	1.57	
MnO	0.01	0.009	0.02	0.008	0.009	0.052	0.256	0.094	0.143	0.016	
Na ₂ O	0.394	0.127	0.118	0.084	0.449	0.458	0.315	0.463	1.23	1.42	
P ₂ O ₅	0.079	0.023	0.065	0.032	0.08	0.122	0.256	0.119	0.147	0.117	

(continued)

Table 5.2 (continued)

Sample	HDP-B12	HDP-B13	HDP-B14	HDP-B15	HDP-B16	HDP-B17	HDP-B18	HDP-B19	HDP-B20	HDP-B21				
TiO ₂	0.299	0.064	0.155	0.058	0.345	0.306	0.142	0.25	0.447	0.548				
LOI	10.41	3.54	6.76	3.56	8.96	10.13	25.17	14.26	12.73	8.03				
Total	99.59	100.12	99.95	100.23	100.26	98.86	96.30	97.10	98.11	98.80				
Al ₂ O ₃ /TiO ₂	27.96	24.53	22.45	25.69	22.29	20.78	22.68	19.28	21.23	24.51				
K ₂ O/N ₂ O	5.61	2.55	7.45	3.86	4.52	3.52	2.55	2.63	1.72	2.30				
CaO*	0.006	0.002	0.002	0.001	0.007	0.007	0.005	0.007	0.020	0.023				
CIA	69.35	67.11	72.17	70.35	67.63	66.15	62.80	62.86	59.96	62.06				
CIAcorr	69.35	67.11	72.17	70.35	67.63	66.15	62.80	62.86	59.96	62.06				
PIA	82.14	74.46	86.68	80.46	78.79	75.38	69.38	69.65	64.02	67.92				
CIW	86.57	78.98	89.96	84.35	83.88	80.84	75.65	75.98	70.10	73.91				
Sample	HDP-B22	HDP-B23	HDP-B24	HDP-B25	HDP-B26	HDP-B27	HDP-B28	HDP-B29	HDP-B30	HDP-B31	HDP-B32	HDP-B33	HDP-B34	PAAS
Longmaxi Formation														
SiO ₂	64.54	49.45	53.36	56.3	65.72	59.6	50.91	42.09	62.85	64.25	51.52	58.53	48.02	62.80
Al ₂ O ₃	10.78	13.64	12.93	11.55	11.15	11.12	10.47	8.88	11.32	12.14	8.14	11.43	11.84	18.90
CaO	3.68	6.65	5.8	5.88	2.9	3.91	6.82	12.22	3.45	2.66	9.35	4.63	9.56	1.30
Fe ₂ O ₃	3.4	3.84	5.73	4.58	3.91	4.66	6.03	4.18	3.83	4.23	3.75	4.16	4.59	7.20
FeO	1.32	1.17	1.39	1.94	1.19	1.66	1.93	2.3	1.55	1.68	1.69	1.29	1.82	-
Fe ₂ O _{3t}	4.87	5.14	7.27	6.74	5.23	6.50	8.17	6.74	5.55	6.10	5.63	5.59	6.61	4.87
K ₂ O	2.48	3.33	3.18	2.7	2.65	2.75	2.58	2.07	2.66	2.85	1.8	2.83	3.13	3.70
MgO	1.72	4.36	2.57	3.03	1.9	2.36	3.98	7.29	2.06	1.87	5.47	2.62	3.42	-
MnO	0.024	0.06	0.038	0.054	0.023	0.033	0.09	0.181	0.024	0.021	0.171	0.044	0.071	2.20
Na ₂ O	1.47	1.35	1.36	1.47	1.38	1.23	1.14	1.1	1.46	1.49	1.3	1.24	0.856	1.20
P ₂ O ₅	0.125	0.101	0.109	0.12	0.118	0.11	0.109	0.109	0.115	0.118	0.125	0.14	0.281	0.16
TiO ₂	0.579	0.495	0.601	0.621	0.581	0.575	0.546	0.448	0.587	0.619	0.442	0.556	0.557	1.00
LOI	9.69	13.58	11.16	10.5	7.58	11.06	12.73	19.89	8.54	7.68	15.33	12.08	15.13	-
Total	99.81	98.03	98.23	98.75	99.10	99.07	97.34	100.76	98.45	99.61	99.09	99.55	99.28	-
Al ₂ O ₃ /TiO ₂	18.62	27.56	21.51	18.60	19.19	19.34	19.18	19.82	19.28	19.61	18.42	20.56	21.26	18.9
K ₂ O/N ₂ O	1.69	2.47	2.34	1.84	1.92	2.24	2.26	1.88	1.82	1.91	1.38	2.28	3.66	3.08
CaO*	0.024	0.022	0.022	0.024	0.022	0.020	0.018	0.018	0.024	0.024	0.021	0.020	0.014	-
CIA	58.88	62.87	62.00	59.79	60.06	61.26	61.51	60.22	59.55	60.29	56.64	61.51	65.59	-
CIAcorr	58.88	62.87	62.00	59.79	60.06	61.26	61.51	60.22	59.55	60.29	56.64	61.51	65.59	-
PIA	62.58	69.30	67.93	64.06	64.57	66.78	67.16	64.70	63.71	64.86	59.12	67.20	74.99	-
CIW	69.03	75.43	74.29	70.48	71.06	73.32	73.62	71.04	70.21	71.23	65.55	73.69	80.78	-

PAAS Post-Archean Average Shale (Taylor and McLennan 1985)

Table 5.3 Analytical data of rare earth elements (ppm) of shales and siltstones from Wufeng-Longmaxi Formations in Huadi no. 1 well

Sample	HDP-B1	HDP-B2	HDP-B3	HDP-B4	HDP-B5	HDP-B6	HDP-B7	HDP-B8	HDP-B9	HDP-B10	HDP-B11
La	52.8	48.8	53.7	50.20	49.8	52.10	36.20	28.60	38.10	48.80	69.00
Ce	115	108	117	105.0	109.0	117.0	76.60	54.50	72.60	103.0	131.0
Pr	11.80	11.20	11.50	11.10	11.5	12.00	8.06	6.44	8.99	13.30	17.50
Nd	42.60	42.40	42.60	42.10	43.40	46.10	30.60	25.00	33.80	50.50	67.70
Sm	7.26	7.20	6.90	7.08	7.98	8.25	6.04	4.75	5.89	8.78	12.50
Eu	1.18	1.23	1.24	1.30	1.52	1.39	1.29	0.86	1.10	1.53	2.13
Gd	6.26	6.48	6.17	6.37	6.77	7.14	5.89	4.09	4.90	7.00	10.20
Tb	1.09	1.09	1.03	1.08	1.21	1.19	1.14	0.75	0.94	1.12	1.72
Dy	5.37	5.54	5.29	5.59	6.04	5.87	6.41	3.90	5.38	6.12	8.88
Ho	1.09	1.12	1.02	1.12	1.23	1.18	1.33	0.76	1.21	1.29	1.72
Er	2.91	3.03	3.00	3.07	3.40	3.27	3.60	2.01	3.45	4.22	5.00
Tm	0.49	0.51	0.46	0.51	0.51	0.56	0.61	0.33	0.61	0.74	0.79
Yb	3.35	3.38	3.19	3.43	3.67	3.57	4.13	2.15	4.29	5.11	5.14
Lu	0.475	0.478	0.465	0.52	0.531	0.567	0.597	0.314	0.624	0.75	0.733
∑REE	251.67	240.46	253.57	238.47	246.57	260.18	182.49	134.45	181.88	252.26	334.01
LREE	230.64	218.83	232.94	216.78	223.20	236.84	158.79	120.15	160.48	225.91	299.83
HREE	21.03	21.63	20.63	21.69	23.37	23.34	23.70	14.31	21.40	26.35	34.18
LREE/HREE	10.97	10.12	11.29	10.00	9.55	10.15	6.70	8.40	7.50	8.58	8.77
La/N/YbN	11.31	10.36	12.07	10.50	9.73	10.47	6.29	9.54	6.37	6.85	9.63
Eu/Eu*	0.54	0.55	0.58	0.59	0.63	0.55	0.66	0.60	0.63	0.60	0.58
Sample	HDP-B12	HDP-B13	HDP-B14	HDP-B15	HDP-B16	HDP-B17	HDP-B18	HDP-B19	HDP-B20	HDP-B21	
La	21.00	5.43	11.9	4.77	28.3	22.8	28.5	21.4	37.3	50.9	
Ce	37.40	9.86	22.1	8.82	44.8	37.4	49.2	36.8	67.8	101	
Pr	4.88	1.30	2.97	1.22	5.75	4.7	6.52	4.35	8.33	12.6	
Nd	19.40	5.42	12.2	5.06	20.4	17.7	26.8	16.7	33.1	47.2	
Sm	3.89	1.05	2.64	1.11	3.71	3.17	5.18	3.17	6.37	8.22	
Eu	0.75	0.25	0.623	0.253	0.67	0.596	1.05	0.592	1.09	1.28	
Gd	3.68	1.01	2.50	1.01	3.30	3.02	4.78	2.94	5.78	6.74	
Tb	0.68	0.20	0.47	0.18	0.61	0.53	0.893	0.523	1.15	1.09	
Dy	3.82	1.08	2.31	1.01	3.42	2.95	4.7	2.79	6.6	5.55	
Ho	0.80	0.21	0.52	0.20	0.75	0.64	0.974	0.546	1.35	1.11	
Er	2.08	0.56	1.27	0.55	2.32	1.80	2.46	1.6	3.87	3.25	

(continued)

Table 5.3 (continued)

Sample	HDP-B12	HDP-B13	HDP-B14	HDP-B15	HDP-B16	HDP-B17	HDP-B18	HDP-B19	HDP-B20	HDP-B21				
Tm	0.35	0.09	0.20	0.08	0.39	0.31	0.369	0.252	0.629	0.489				
Yb	2.47	0.631	1.31	0.562	2.58	1.98	2.38	1.55	4.36	3.26				
Lu	0.355	0.086	0.186	0.072	0.432	0.29	0.322	0.233	0.598	0.491				
∑REE	101.55	27.17	61.19	24.89	117.43	97.88	134.13	93.45	178.33	243.18				
LREE	87.32	23.31	52.43	21.23	103.63	86.37	117.25	83.01	153.99	221.20				
HREE	14.23	3.86	8.76	3.66	13.80	11.52	16.88	10.43	24.34	21.98				
LREE/HREE	6.13	6.04	5.99	5.80	7.51	7.50	6.95	7.96	6.33	10.06				
LaN/YbN	6.10	6.17	6.52	6.09	7.87	8.26	8.59	9.90	6.14	11.20				
Eu/Eu*	0.60	0.75	0.74	0.73	0.59	0.59	0.65	0.59	0.55	0.53				
Sample	HDP-B22	HDP-B23	HDP-B24	HDP-B25	HDP-B26	HDP-B27	HDP-B28	HDP-B29	HDP-B30	HDP-B31	HDP-B32	HDP-B33	HDP-B34	PAAS
La	41.4	47.1	42	44.1	39.2	38.1	37.5	36.9	43.5	41.9	46.6	52.5	38.2	
Ce	76.9	89.8	77.1	78.5	73.7	69	68.3	64.6	77	75.5	85.5	84.9	79.6	
Pr	9.42	11	9.33	9.47	9.01	8.21	8.1	7.8	9.78	9.27	7.45	10.4	8.83	
Nd	36.3	40.6	35.6	36.3	35.4	31.9	31.9	30.5	37.1	35.9	29	38.3	33.9	
Sm	6.65	7.37	6.43	6.75	6.37	5.71	5.73	5.81	7.02	6.4	5.62	6.96	5.55	
Eu	1.12	1.47	1.21	1.2	1.15	1.03	1.05	1.03	1.16	1.03	1.01	1.25	1.08	
Gd	5.73	6.26	5.56	6.04	5.5	5.02	5.06	4.88	6.2	5.6	4.7	6.32	4.66	
Tb	0.997	1.04	0.968	1.06	0.951	0.885	0.864	0.886	1.02	0.958	0.874	1.09	1.06	
Dy	5.36	5.59	5.13	5.39	4.83	4.65	4.67	4.84	5.55	4.86	4.63	5.83	4.68	
Ho	1.05	1.12	1.01	1.11	0.933	0.927	0.945	0.934	1.12	1	0.89	1.16	0.99	
Er	3.01	3.34	3.03	3	2.67	2.54	2.67	2.56	3.04	2.77	2.47	3.33	2.85	
Tm	0.493	0.542	0.466	0.479	0.379	0.402	0.423	0.413	0.501	0.433	0.418	0.542	0.41	
Yb	3.06	3.38	3.05	3.1	2.61	2.7	2.65	2.72	3.11	2.91	2.62	3.38	2.82	
Lu	0.447	0.534	0.437	0.474	0.375	0.386	0.382	0.382	0.489	0.399	0.369	0.537	0.43	
∑REE	191.94	219.15	191.32	196.97	183.08	171.46	170.24	164.26	196.59	188.93	155.85	211.48	184.77	
LREE	171.79	197.34	171.67	176.32	164.83	153.95	152.58	146.64	175.56	170.00	138.88	189.29	167.16	
HREE	20.15	21.81	19.65	20.65	18.25	17.51	17.66	17.62	21.03	18.93	16.97	22.19	17.61	
LREE/HREE	8.53	9.05	8.74	8.54	9.03	8.79	8.64	8.32	8.35	8.98	8.18	8.53	9.49	
LaN/YbN	9.70	10.00	9.88	10.20	10.77	10.12	10.15	9.73	10.03	10.33	9.61	9.89	12.64	
Eu/Eu*	0.55	0.66	0.62	0.57	0.59	0.59	0.60	0.59	0.54	0.53	0.60	0.58	0.65	

Stage, and volcanic ash fell to the surface of the ocean and provided nutrients for life to flourish. The Yangtze Block ended the carbonate deposition and began to sediment the black shales of the Wufeng Formation by the integrated control of multiple factors. In the early Hirnantian, because of the sustained collision, the basin base continued to decline. However, global glaciation started, ice constantly formed, and the global sea level decreased. Since the falling rate of the basin base was greater than the descent of the sea level caused by the glaciation, and the volcanic eruption events were fewer than before, the increase in nutrients decreased, and the sea level in the Upper Yangtze region constantly increased. Thus, black shales with relatively low TOC values were still deposited in the upper part of the Wufeng Formation in the Yangtze area. In the middle Hirnantian, the compression between the Yangtze and Cathaysia blocks continued, and the basin basement declined. The falling rate of the basin base was less than the descent of the sea level caused by the glaciation, and the relative sea

level decreased, depositing the siltstones of the Guanyinqiao Formation. In the late Hirnantian, the sea-level change was the same as that in the early Hirnantian period, and the relative sea level increased. Black shales were deposited in the lower part of the Longmaxi Formation. In the Rhuddanian (early Silurian), the basin basement declined continuously, the glaciation ended, and the global sea level increased. A new round of frequent volcanic eruptions resumed, providing more nutrition for creatures on the surface of the ocean. The combination of the three factors promoted the increase in the sea level, and black shales were deposited in the lower part of the Longmaxi Formation (Fig. 5.10). According to these studies, although both the Wufeng and Longmaxi Formations developed the same black shales, the formation mechanisms were different. In terms of the factors controlling the organic matter enrichment and preservation, apart from the black shale and ancient seawater water environment, the effect of volcanic activity and glaciation cannot be ignored. Tectonic

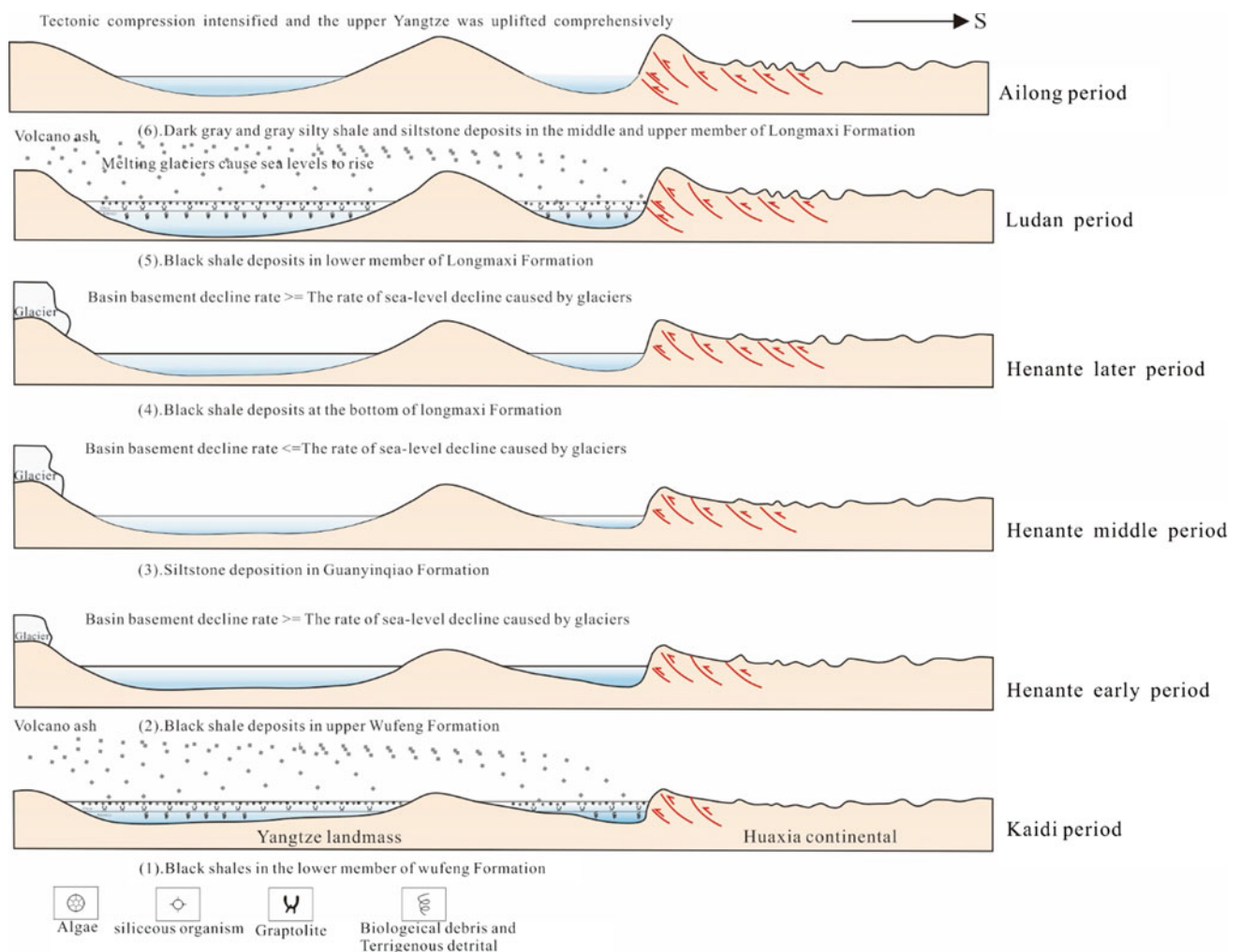


Fig. 5.10 Sedimentary mode of the black shales from the Wufeng and Longmaxi Formations in Sichuan basin

compression resulted in the descending basin basement, and an anoxic water environment was generated. The black shales of the Wufeng Formation were deposited. Notably, the black shales of the Longmaxi Formation were deposited after glacier ablation, and the combination of ablation and tectonic compression led to the increase in sea level and accelerated the formation of an anoxic environment, thereby promoting the burial and preservation of black organic matter.

References

- Brenchley PJ, Marshall JD, Harper DAT et al (2006) A late Ordovician (Hirnantian) karstic surface in a submarine channel, recording glacioeustatic sea-level changes: Meifod, central Wales. *Geol J* 41:1–22
- Chen X, Fan JX, Wang WH et al (2017) Stage-progressive distribution pattern of the Lungmachi black graptolitic shales from Guizhou to Chongqing, Central China. *Scientia Sinica (Terrae)* 47(6):720–732
- Condie KC, Boryta MD, Liu JZ et al (1992) The origin of khondalites: geochemical evidence from the Archean to early proterozoic granulite belt in the North China craton. *Precamb Res* 59:207–223
- Fedo CM, Nesbitt HW, Young GM (1995) Unraveling the effects of Kmetasomatism in sedimentary rocks and paleosols with implications for palaeoweathering conditions and provenance. *Geology* 23:921–924
- Fu XG, Wang J, Chen WB et al (2015) Organic accumulation in lacustrine rift basin: constraints from mineralogical and multiple geochemical proxies. *Int J Earth Sci* 104:495–511
- Ge XY, Mou CL, Wang CS et al (2019a) Mineralogical and geochemical characteristics of K-bentonites from the Late Ordovician-Early Silurian in South China and their geological significance. *Geol J* 54:514–528
- Ge XY, Mou CL, Yu Q et al (2019b) The geochemistry of the sedimentary rocks from the Well Huadi No. 1 in the Wufeng-Longmaxi Formations (Upper Ordovician-Lower Silurian), South China, with implications for paleoweathering, provenance, tectonic setting and paleoclimate. *Mar Pet Geol* 103:646–660
- Harnois L (1988) The CIW index: a new chemical index of weathering. *Sediment Geol* 55:319–322
- Harper DAT, Hammarlund EU, Rasmussen CMØ (2014) End Ordovician extinctions: a coincidence of causes. *Gondwana Res* 25:1294–1307
- Lee YI (2009) Geochemistry of shales of the upper cretaceous Hayang group, SE Korea: implications for provenance and source weathering at an active continental margin. *Sed Geol* 215:1–12
- Ma PF, Wang LC, Wang CS et al (2015) Organic-matter accumulation of the lacustrine lunpola oil shale, central Tibetan plateau: controlled by the paleoclimate, provenance, and drainage system. *Int J Coal Geol* 147–148:58–70
- Moosavirad SM, Janardhana MR, Sethumadhav MS et al (2011) Geochemistry of lower Jurassic shales of the Shemshak Formation, Kerman Province, Central Iran: provenance, source weathering and tectonic setting. *Chemie Dre Erde Geochem* 71:279–288
- Mou CL, Ge XY, Yu Q et al (2019) Palaeoclimatology and provenance of black shales from Wufeng- Longmaxi Formations in south-western Sichuan Province: from geochemical records of Well Xindi-2. *J Palaeogeogr* 21(5):835–854
- Nesbitt HW, Young GM (1982) Early proterozoic climates and plate motions inferred from major element chemistry of lutites. *Nature* 299:715–717
- Nesbitt HW, Young GM (1984) Prediction of some weathering trends of plutonic and volcanic rocks based on thermodynamic and kinetic considerations. *Geochim Cosmochim Acta* 48(7):1523–1534
- Nesbitt HW, Young GM (1989) Formation and diagenesis of weathering profiles. *J Geol* 97:129–147
- Qiu Z, Zou CN (2020) Unconventional petroleum sedimentology: connotation and prospect. *Acta Sedimentol Sin* 38(01):1–29
- Rong JY, Zan RB (1999) Ordovician-Silurian Brachiopod Fauna Turnover in South China. *Geoscience* 13(4):390–394
- Rong JY (1999) Ordovician-Silurian Brachiopod Turnover in south china. *Geoscience* 02:74
- Taylor SR, McLennan SM (1985) The continental crust: its composition and evolution. Blackwell, UK, Oxford, Blackwell
- Yan DT, Chen DZ, Wang QC et al (2010) Large-scale climatic fluctuations in the latest Ordovician on the Yangtze block, South China. *Geology* 38:599–602
- Young GM, Nesbitt HW (1998) Processes controlling the distribution of Ti and Al in weathering profiles, siliciclastic sediments and sedimentary rocks. *J Sediment Res* 68(3):448–455

Open Access This chapter is licensed under the terms of the Creative Commons Attribution-NonCommercial-NoDerivatives 4.0 International License (<http://creativecommons.org/licenses/by-nc-nd/4.0/>), which permits any noncommercial use, sharing, distribution and reproduction in any medium or format, as long as you give appropriate credit to the original author(s) and the source, provide a link to the Creative Commons license and indicate if you modified the licensed material. You do not have permission under this license to share adapted material derived from this chapter or parts of it.

The images or other third party material in this chapter are included in the chapter's Creative Commons license, unless indicated otherwise in a credit line to the material. If material is not included in the chapter's Creative Commons license and your intended use is not permitted by statutory regulation or exceeds the permitted use, you will need to obtain permission directly from the copyright holder.

